

Optical feedback laser absorption spectroscopy of N<sub>2</sub>O at 2 μmT.A. Odintsova<sup>a,b</sup>, E. Fasci<sup>a,c</sup>, S. Gravina<sup>a</sup>, L. Gianfrani<sup>a,c</sup>, A. Castrillo<sup>a,\*</sup><sup>a</sup> Dipartimento di Matematica e Fisica, Università della Campania "Luigi Vanvitelli", Caserta, Italy<sup>b</sup> The Institute of Applied Physics of the Russian Academy of Sciences, Nizhny Novgorod, Russia<sup>c</sup> INFN, Istituto Nazionale di Fisica Nucleare, Sez. di Napoli, Complesso Universitario di M.S. Angelo, Via Cintia, 80126 Napoli, Italy

## ARTICLE INFO

## Article history:

Received 19 April 2020

Revised 24 June 2020

Accepted 25 June 2020

Available online 26 June 2020

## Keywords:

Nitrous oxide

Line intensities

Hartmann-Tran profile

Frequency-comb-assisted OF-LAS

## ABSTRACT

We present high-accuracy measurements of the spectroscopic parameters of eight nitrous oxide transitions, mainly belonging to the P branch of the  $3\nu_1 + 2\nu_2$  vibrational band, in the spectral region around  $4982\text{ cm}^{-1}$ . We acquired absorption spectra in pure N<sub>2</sub>O samples, at room-temperature, by means of a diode laser based spectrometer in which the laser emission width was effectively narrowed by exploiting the optical feedback from a V-shaped high-finesse cavity. The spectrometer was assisted by a self-referenced optical frequency comb synthesizer for frequency calibration purposes. Light absorption from N<sub>2</sub>O molecules occurred inside a multiple reflections cell, which was placed on the transmission from the cavity. The successful application of a global fitting approach to a manifold of spectra, involving the symmetric uncorrelated version of quadratic speed-dependent hard collision profile, allowed us to determine line intensities with an overall relative uncertainty of 0.38%. We found a satisfactory agreement with data provided by the HITRAN and NODS-1000 databases. Self-broadening coefficients, speed dependence components of the collisional line broadening, and Dicke narrowing parameters were also determined.

© 2020 Elsevier Ltd. All rights reserved.

## 1. Introduction

Nitrous oxide (N<sub>2</sub>O), a gas included in the N<sub>x</sub>O<sub>y</sub> oxides family, is a minor constituent of the atmosphere. It originates near the Earth's surface mainly from the decay of organic material under anaerobic conditions and is removed from the stratosphere by photo dissociation. Human activities, such as agriculture and fuel combustion, are causing an increase of atmospheric N<sub>2</sub>O mixing ratio [1]. Albeit its concentration remains at the trace amount level (0.33 ppm), nitrous oxide is effectively enhancing the greenhouse effect and influencing the global climate. In fact, it is recognized to be the third most important "dry" greenhouse gas after CO<sub>2</sub> and CH<sub>4</sub> [2]. It strongly influences the troposphere heat budget. In particular, the increase of its anthropogenic emissions is leading to a significant increase of the Earth's surface temperature [3]. This effect is further amplified by the fact that N<sub>2</sub>O is a long-lived molecule. In fact, its average atmospheric residence time has been quantified to be about 116 years [4]. Another debated question is related to the relative strength of N<sub>2</sub>O sources. Although the amount of total emissions is well quantified, the relative contribution of each source remains largely unknown, due to the complexity of the pathways involved [5]. Likewise, there is an important

role of N<sub>2</sub>O in the nitrogen oxide catalyzed process that entail the ozone destruction in the stratosphere [6]. High-quality and accurate N<sub>2</sub>O concentration measurements appear to be an indispensable tool for further understanding of the role of nitrous oxide at the tropospheric level as well as for studies devoted to quantification of its circulation in the middle atmosphere.

Several ground- and satellite-based missions have been dedicated to remote measurements of atmospheric concentration and vertical columns of N<sub>2</sub>O. As far as ground-based missions are concerned, we can surely cite the Total Carbon Column Observing Network (TCCON) [7] and the Network for the Detection of Atmospheric Composition Change (NDACC) [8]. On the other hand, the Aura Microwave Limb Sounder (MLS) instrument represents one of the most important examples of satellite-based mission [9].

To successfully complete the work for which they have been designed, these missions necessitate of the accurate knowledge of N<sub>2</sub>O spectroscopic parameters. In particular, data regarding line intensities are of utmost importance since they are required to retrieve the amount fractions of N<sub>2</sub>O from measured spectra. Hence, to ensure the reliability of remote measurements, it is desirable to assess the line strengths of the investigated transitions with the highest accuracy and a well-defined uncertainty budget.

So far, the majority of nitrous oxide spectroscopic data that are available in the literature have been obtained by means of Fourier Transform Spectrometers (FTS) [10–18]. In these experiments, several spectral windows have been investigated and

\* Corresponding author.

E-mail address: [antonio.castrillo@unicampania.it](mailto:antonio.castrillo@unicampania.it) (A. Castrillo).

extensive lists of transition frequencies, line intensities, and pressure-broadening coefficients have been obtained [10–12]. Moreover, in Refs. [13,14] the authors have also derived line mixing coefficients and speed dependence parameters for the  $\nu_3$  fundamental band at  $4.5\mu\text{m}$ . Usually, line strengths have been derived with large uncertainties, ranging between 2 and 5%. Only recently, motivated by the purposes of the TCCON mission, Werwein and co-workers have been successful in pushing down to a sub-percent level the uncertainty on  $\text{N}_2\text{O}$  line strengths [17], self-broadening, and shifting coefficients [16]. It is worth noting that the vast majority of spectroscopic data reported in the HITRAN database [19] comes from the extensive study of Ref. [10].

Recently, cavity-ring down spectroscopy experiments have been performed for the investigation of several high-energy  $\text{N}_2\text{O}$  absorption bands in the spectral regions between  $6950\text{--}7653$  and  $7915\text{--}8334\text{cm}^{-1}$  [20–22]. Line intensities and center frequencies have been retrieved for a manifold of spectral lines by means of a global fitting code based on the use of a Voigt profile. However, in the most favorable cases of relatively strong and well-isolated transitions, the authors estimated the accuracy of line intensities determinations to be in the 4–7% range [21]. In other cases, when the weakness of the lines was a limiting factor, the averaged accuracy was inferred to be about 20% or worse [22].

In the last release of the HITRAN database [19], the authors have discussed the inadequacy of the Voigt profile in representing the shapes of individual transitions in molecular spectra at atmospheric conditions. For this reason, the HITRAN community has proposed the inclusion of a new series of parameters in the database for modeling absorption spectra by means of more sophisticated line shape models. These parameters are the speed dependence coefficient for collisional broadening, the frequency of velocity changing collisions, the correlation parameter, and the first-order line mixing coefficient (see Table 2 of Ref. [19]). Until now, this inclusion has started only for few selected molecules, such as  $\text{H}_2$  [23],  $\text{O}_2$  [24], and for few transitions of  $\text{H}_2\text{O}$ ,  $\text{CO}$ ,  $\text{HF}$ , and  $\text{HCl}$ . In the case of nitrous oxide, benefiting of the results of Ref. [13], only the spectral range  $2184.8$  to  $2251.6\text{cm}^{-1}$  has been covered, thus revealing the need of further investigations at different wavelengths.

In this paper, we report on the accurate measurements of  $\text{N}_2\text{O}$  line intensities by means of optical-feedback laser absorption spectroscopy (OF-LAS). Assisted by an optical frequency comb, the cavity-based diode laser spectrometer is an upgraded version of the apparatus used for measurements of the R-branch of the  $\nu_1 + 2\nu_2 + \nu_3$   $\text{CO}_2$  band [25]. The OF-LAS method builds upon the seminal idea of Optical-Feedback Cavity-Enhanced Absorption Spectroscopy (OF-CEAS) [26]. Compared to OF-CEAS, our method is less sensitive but more accurate, due to the difficulties of OF-CEAS in retrieving the absorption coefficient from the transmission maxima [27]. The main features of our spectrometer are the narrow spectral width of the laser radiation probing the lines of interest and the highly accurate frequency scale underneath the absorption spectra. A global fitting approach, involving the symmetric and uncorrelated version of the Hartmann-Tran profile [28], is applied to a manifold of spectra, which are simultaneously analyzed across a given range of pressures, sharing a restricted number of unknown parameters. So doing, for all the investigated transitions, we determine additional spectroscopic parameters, such as self-broadening coefficient, speed dependence component of the collisional line broadening, and Dicke narrowing parameter.

The paper is organized as follows: Section 2 describes the experimental setup; Section 3 deals with the line shape analysis. The strategy for path length determination is discussed in Section 4, while Section 5 shows the results. Section 6 reports on the overall uncertainty budget on line intensity determinations. Conclusions are the subject of Section 7.

## 2. Experimental setup

The experimental setup used for the present study, shown in Fig. 1, is similar to that described in Ref. [25]. Here, we give a description of the spectrometer, focusing on those experimental tricks that represent elements of novelty and that are of particular interest for the  $\text{N}_2\text{O}$  line strength determinations. Very briefly, the setup includes four main parts: (i) an external-cavity diode laser optically locked to a high-finesse cavity, (ii) a multiple reflections cell (MRC) where the laser-gas interaction takes place, (iii) a comb-assisted frequency calibration unit, and (iv) an additional part expressly developed for the determination of the MRC path length.

The first part consists of a V-shaped cavity, with two equal-length arms of about  $52.4\text{ cm}$ , and a distributed feedback diode laser (DFB-DL1, in Fig. 1), operating at  $2.007\mu\text{m}$ , that is optically locked to the cavity. In this configuration a substantial reduction of the laser linewidth can be achieved exploiting the optical feedback (OF) from the cavity to the laser. In fact, taking advantage of the same principle of operation of the OF-CEAS technique described in Ref. [26], the laser linewidth could be reduced by more than two order of magnitude, namely from  $2\text{ MHz}$  (in free running condition) down to about  $10\text{ kHz}$ , namely at the level of the cavity mode width. This is accomplished if the laser can benefit of selective OF from the intracavity field: when the laser frequency matches that of the cavity resonances, OF guarantees superior performances of the laser in terms of its emission width, provided that optimal values of the OF rate and optical phase are properly maintained [26]. The fraction of the light returning to the laser, the OF rate, is controlled by a combination of a half-wave plate and a linear polarizer. The optical phase, which is determined by laser-cavity distance, is adjusted in real time by a steering mirror mounted on a piezo actuator actively controlled by an electronic feedback circuit. The circuit looks at the symmetry of cavity modes and produces an error signal, which is fed to the piezo for fine adjustments of mirror position in order to fulfil a constructive interference condition. In our setup, laser-cavity distance matches exactly the length of each cavity arms, so that the light transmitted by the cavity can be sampled at the even as well as odd longitudinal cavity modes, which are spaced in frequency by exactly one cavity free spectral range (FSR). In particular, when the laser frequency is linearly ramped over the desired spectral range, the OF leads to a transient locking of the laser to the cavity, thus allowing for a stepwise laser frequency scan in correspondence of each successive cavity modes. High-vacuum level is guaranteed in the cavity, during laser scans. Thus, the light emerging from the cavity has a pattern like the one of a stable comb structure in which two equidistant consecutive teeth are separated by exactly one FSR. This occurrence holds at both the end mirrors, regardless of the cavity arm, making this comb-like shape available in two different paths. In particular, the one leaving from the first mirror is immediately monitored by means of an extended-wavelength InGaAs fast photodetector having a detection bandwidth of about  $1.5\text{ MHz}$  (FPD1, in Fig. 1), while the other is used to probe the  $\text{N}_2\text{O}$  gas samples.

Laser-gas interaction takes place in a Herriott-type multiple reflections cell. Mounted in a 48-pass configuration, the MRC has a nominal path length of about  $20.5\text{ m}$ . It is equipped with a thermometer and a capacitive absolute pressure gauge, for temperature and pressure measurements respectively. In particular, temperature is monitored by a Pt-100 platinum resistance thermometer mounted on the external surface of the glass cell, whose resistance is recorded by means of a  $6\frac{1}{2}$  resolution multimeter (Keithley, model 2700). Gas pressure is measured using a 100-Torr full-scale manometer (MKS Baratron, model 690A12TRA), having an accuracy of 0.05% of the reading, directly connect to the MRC. A  $\text{N}_2\text{O}$  gas bottle, with a quoted purity of 99.0%, provides gaseous samples

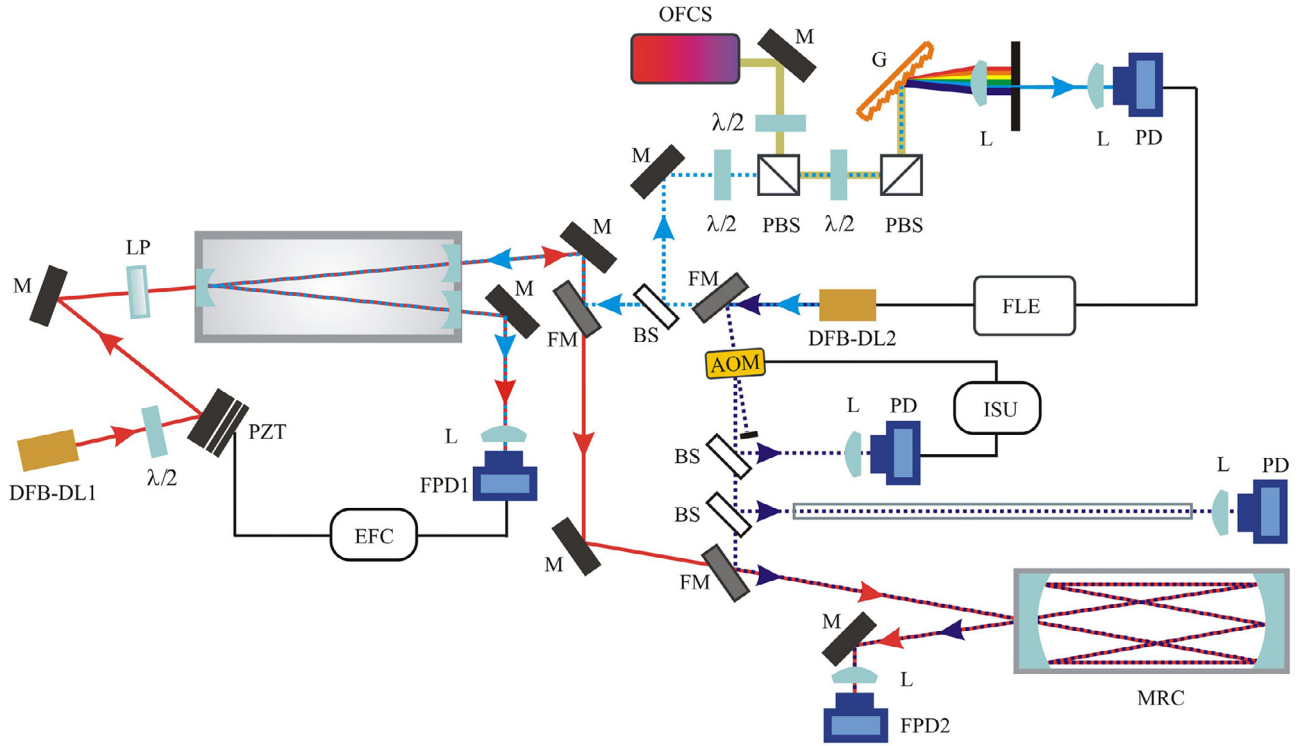


**Fig. 1.** Sketch of the experimental setup: DFB-DL stands for distributed feedback diode laser, M for mirror, BS for beam splitter, FM for flipping mirror, L for lens,  $\lambda/2$  for half-wave plate, LP for linear polarizer, PZT for piezoelectric transducer, EFC for electronic feedback circuit, PD for large area photodetector, FPD for fast photodiode, OFCS for optical frequency comb synthesizer, PBS for polarizing beam splitter, G for grating, FLE for frequency locking electronics, AOM for acousto-optic modulator, ISU for intensity stabilization unit, MRC for multiple reflections cell. Laser beam paths marked by red, light blue, and dark blue colors correspond to three sections of the setup: that developed for  $\text{N}_2\text{O}$  spectroscopic parameters determination, the comb-assisted frequency calibration unit, and the section developed for the MRC path length determination, respectively. Black lines are for electrical connections. (For interpretation of the references to colour in this figure legend, the reader is referred to the web version of this article.)

for the experiment. A turbo-molecular pump is used to periodically evacuate the cell and create high-purity conditions. A second fast photodiode (FPD2), having similar characteristics of the previous, is used to monitor the power transmitted from the MRC. Signals from both photodetectors, namely the one monitoring the cavity output and the other emerging from the MRC, are simultaneously recorded by an acquisition board (Gage, model CSE1622), working at a sample rate of  $10^6$  Samples/s and with a vertical resolution of 16 bit. For each of the two channels, more than 200,000 points are recorded. A LABVIEW code controls the acquisition card, retrieves the maximum value for each of the cavity resonance recorded by the two detectors, calculates the logarithm of their ratio, and acquire the temperature of the MRC in correspondence of each frequency scan.

The third part of the setup is the frequency calibration unit, which is expressly developed for a low-uncertainty measurement of the cavity FSR. The procedure we follow for FSR determination, extensively described in Ref. [25], consists in the use of a secondary 2- $\mu\text{m}$  diode laser (DFB-DL2, in Fig. 1) coupled to the V-cavity and frequency locked to the nearest tooth of a self-referenced optical frequency comb synthesizer (OFCS, MENLO SYSTEM FC1500-250-ULN). This latter is fully stabilized against the frequency of a Rb-clock. Laser frequency scans are performed changing the repetition rate frequency of the OFCS, while the carrier-envelope offset frequency remained locked to a proper radio-frequency signal. From the analysis of several interference profiles (i.e. Airy functions), recorded under high-vacuum conditions by FPD1 during comb-assisted frequency scans of DFB-DL2, we determine a FSR of  $(4.6179 \pm 0.0010) \times 10^{-3} \text{ cm}^{-1}$ . We use this value for the calibration of the frequency scale underneath the  $\text{N}_2\text{O}$  experimental spectra. It must be pointed out that no effects due to

dispersion introduced by the high-reflectivity coatings of the mirrors are evidenced in the measurement of the FSR.

The last part of the setup is used for the accurate measurement of the MRC path length, according to the procedure described in Section 4. In a few words, the laser beam provided by DFB-DL2 is switched from the high-finesse cavity to the MRC, by using a flipping mirror. Before entering the absorption cell, a series of beam-splitters divide the beam in two extra portions of nearly equal intensities. The first goes to a monitor detector, whose output signal is used to actively stabilize the laser power by means of an acousto-optic modulator, while the second is aligned into a 1-m long reference cell. For the aims of this measurement, FPD2 is replaced with a large-area extended-wavelength InGaAs detector having a bandwidth of  $\sim 15 \text{ kHz}$ . Laser radiation emerging from the MRC and reference cell is simultaneously monitored. The detector at the output of the reference cell is identical to the one used for the MRC. A turbo-molecular pump provides vacuum conditions in both the cells, whereas a needle valve is used for high-precision gas injection. The two cells are connected to each other with a 10-cm long DN-16 stainless steel tube (not shown in Fig. 1). This assures that the absorption processes can take place with the gas samples at exactly the same thermodynamic conditions.

### 3. Line shape analysis

According to the Beer-Lambert law, the absorbance as function of the laser frequency  $\tilde{A}(\tilde{\nu}, T)$ , is the ratio of light intensity after passing through the gaseous sample,  $I(\tilde{\nu})$ , and the initial light intensity,  $I_0(\tilde{\nu})$ , in a common logarithm scale, as shown below:

$$\tilde{A}(\tilde{\nu}, T) = -\ln \left[ \frac{I(\tilde{\nu})}{I_0(\tilde{\nu})} \right] = S(T)g(\tilde{\nu} - \tilde{\nu}_0)NL, \quad (1)$$

being  $S(T)$  the line strength (in cm/molecule) at a given temperature,  $T$ ,  $g(\tilde{\nu} - \tilde{\nu}_0)$  the normalized line shape function (in cm),  $\tilde{\nu}_0$  the line center frequency (in  $\text{cm}^{-1}$ ),  $N$  the molecular number density (in molecules/ $\text{cm}^3$ ), and  $L$  the absorption path length (in cm). We must note that in our experiment  $I(\tilde{\nu})$  is collected at the output of the MRC, whereas  $I_0(\tilde{\nu})$  is the signal recorded at the cavity output (see Section 2).

For a given absorption spectrum, in coincidence with a certain molecular transition, the integrated absorbance,  $A(T)$ , can be used to retrieve the line strength parameter, provided that a nonlinear least-squares fit of an experimental profile to a given line shape model is performed. We remind that  $A(T)$  is defined as the integral over frequency of Eq. (1) according to the formula:

$$A(T) = \int_{-\infty}^{\infty} -\ln \left[ \frac{I(\tilde{\nu})}{I_0(\tilde{\nu})} \right] d\tilde{\nu} = S(T)NL. \quad (2)$$

Moreover, other parameters, including the line centre frequency and the pressure broadening coefficient, can be easily inferred. Nevertheless, for accurate and high-quality determinations of these parameters, refined line shape models, accounting for broadening and narrowing mechanisms that affect the absorption profiles, must be used. Several studies, performed at different wavelengths and on different molecular targets, such as  $\text{H}_2\text{O}$  [29,30],  $\text{C}_2\text{H}_2$  [31,32] and  $\text{CO}_2$  [33,34], have clearly shown that it is crucial to properly take into account speed-dependence and Dicke narrowing effects for accurate retrievals of line strengths. Recently, the partially correlated quadratic speed-dependent hard collision profile, also known as the Hartmann-Tran (HT) profile [28], has been attracting considerable attention from the spectroscopic community. Proposed as the standard modelling function for high-resolution spectra analysis [35], it has also been implemented in the last version of the HITRAN database for spectra simulations. Moreover, recently, Konefal and co-workers have proposed a new version of the HT profile, called  $\beta$ -corrected HT ( $\beta$ HT) profile [36]. Here, a correction to the frequency of the velocity-changing collisions,  $\nu_{VC}$ , of the hard-collision model adopted in the HT profile is introduced in order to interpret those situations in which the Dicke narrowing effect is dominant and the HT profile fails, providing unphysical results for  $\nu_{VC}$ . More particularly, the  $\beta$ HT profile constitutes an approximation of the so-called partially correlated speed-dependent billiard-ball (pcSDBB) profile [37], which takes into account the mass ratio of colliding molecules and models the relative importance of speed- and direction-changing collisions. It is worth noting that the  $\beta$ HT model, as the original HT profile, has an important advantage over the pcSDBB model because it can be easily and rapidly computed, as it is expressible in terms of two complex probability functions. In fact, the correction introduced to the frequency of the velocity-changing collisions is obtained by multiplying  $\nu_{VC}$  by an analytical function,  $\beta_\alpha$ , defined by Konefal et al. [36]:

$$\beta_\alpha = A_\alpha \tanh(B_\alpha \log_{10} \chi + C_\alpha) + D_\alpha \quad (3)$$

where

$$A_\alpha = 0.0534 + 0.1585e^{-0.4510\alpha} \quad (4a)$$

$$B_\alpha = 1.9595 - 0.1258\alpha + 0.0056\alpha^2 + 0.0050\alpha^3 \quad (4b)$$

$$C_\alpha = -0.0546 + 0.0672\alpha - 0.0125\alpha^2 + 0.0003\alpha^3 \quad (4c)$$

$$D_\alpha = 0.9466 - 0.1585e^{-0.4510\alpha} \quad (4d)$$

being  $\alpha$  the perturber-to-absorber mass ratio (equal to 1 in the case of  $\text{N}_2\text{O}$  self-colliding molecules) and  $\chi$  the ratio of  $\nu_{VC}$  to the

Doppler width,  $\Gamma_D$ . An important point is that the  $\beta_\alpha$  correction does not add any extra parameter to the line shape model.

For the sake of simplicity, we refer the reader to Refs. [28,36] for the complete set of equations describing the HT and  $\beta$ HT profiles. Here, we want to recall that the  $\beta$ HT profile makes use of the following eight parameters:

$$\beta\text{HT} = \beta\text{HT}(\tilde{\nu}_0, \Gamma_D, \Gamma_0, \Delta_0, \gamma_2, \delta_2, \beta_\alpha \nu_{VC}, \eta), \quad (5)$$

where  $\Gamma_0$  and  $\Delta_0$  are, respectively, the collisional width and shift averaged over molecular speed,  $\gamma_2$  and  $\delta_2$  are dimensionless parameters accounting for the speed dependence of collisional broadening and shifting,  $\beta_\alpha \nu_{VC}$  represents the corrected effective frequency of velocity changing collisions, and  $\eta$  is the correlation parameter.

It is worth noting that the majority of the most common line shape models can be easily deduced from Eq. (5). In particular, if instead of using Eq. (3)  $\beta_\alpha$  is set equal to 1, the  $\beta$ HT becomes the usual HT profile. If  $\beta_\alpha=1$  and  $\eta=0$ , it is converted in the quadratic speed-dependent hard collision (qSDHC) profile. Fixing both  $\eta$  and  $\nu_{VC}$  to zero, the quadratic speed-dependent Voigt (qSDV) profile is derived. We anticipate that in the analysis of the experimental spectra of this study, we use the uncorrelated and symmetric versions of these profiles, namely we set equal to zero  $\Delta_0$ ,  $\delta_2$ , and  $\eta$ .

The shape of a molecular transition is  $g(\tilde{\nu} - \tilde{\nu}_0) = \text{Re}[\beta\text{HT}]$ . In order to take into account line mixing (LM) effects, according to the first-order approximation proposed in Ref. [38],  $g(\tilde{\nu} - \tilde{\nu}_0)$  should be modified following this equation:

$$g(\tilde{\nu} - \tilde{\nu}_0) = \text{Re}[\beta\text{HT}] + Y \text{Im}[\beta\text{HT}], \quad (6)$$

being  $\text{Im}[\ ]$  the imaginary part of the quantity in parenthesis,  $Y = p\zeta$  the first-order line mixing parameter,  $p$  the gas pressure, and  $\zeta$  the line mixing pressure-normalized coefficient (commonly in  $\text{atm}^{-1}$ ). This last parameter accounts for the collisional coupling between the considered transition and the others. We have also included LM in the analysis of the experimental spectra. Hereafter, the suffix LM, after the acronyms of a particular line shape, will denote the inclusion of line mixing in the spectral analysis.

Finally, the dependence of the collisional width on molecular speed,  $\nu_a$ , is considered in a quadratic form, namely  $\Gamma(\nu_a) = \Gamma_0\{1 + \gamma_2[(\nu_a/\nu_{a0})^2 - 3/2]\}$ ,  $\nu_{a0}$  being the most probable speed of the molecules [39].

The experimental values of the absorbance are compared with the following function:

$$\tilde{A}(\tilde{\nu}, T) = (P_0 + P_1 \tilde{\nu}) \times \sum_{i=1}^n A_i(T) g_i(\tilde{\nu} - \tilde{\nu}_{0i}) \quad (7)$$

where  $P_0$  and  $P_1$  are the intercept and slope of a linear background accounting for a possible residual variation of the laser power, while  $n$  indicates the number of lines that have been recorded in a single laser frequency scan. Therefore, for the line pairs P(42) and R(6), P(43) and R(4), and R(7) and P(43), the  $n$ -index in the summation of Eq. (7) is equal to 2, while  $n=1$  for the isolated transitions (see Table 1).

For each line, 19 different pressures, ranging from 5 to about 100 Torr, are recorded. For each pressure, 100 repeated spectral acquisitions are performed, so that 1900 experimental profiles has to be analysed. The application of Eq. (7) for modelling a single experimental spectrum is not suitable with all the parameters floating, due to statistical correlation issues that could make the fit critical and unstable. In order to mitigate this difficulty, we apply a multispectrum fitting procedure [40]. In this approach, some of the line shape parameters could be shared among all the spectra, thus providing physical constraints. This is the case of the collisional width  $\Gamma_0$ , the  $\gamma_2$  parameter, the effective frequency of velocity changing collisions, the  $\eta$ , and  $Y$  parameters, for each line of any



**Table 1**

Investigated N<sub>2</sub>O lines, with their transition wavenumbers, vibrational assignments, and lower state energies. Data are taken from the HITRAN database [19]. Last column reports the temperature at which experimental spectra have been recorded, along with the 1- $\sigma$  statistical uncertainty.

Line	Transition	Wavenumber (cm <sup>-1</sup> )	Vibrational assignment	Lower state energy, E'' (cm <sup>-1</sup> )	Temperature (K)
a	P(41)	4984.29084	3v <sub>1</sub> +2v <sub>2</sub>	721.0147	297.57(18)
b	R(7)	4983.92241	v <sub>2</sub> <sup>1</sup> +2v <sub>3</sub>	23.4641	297.00(17)
c	P(43)	4983.76336	3v <sub>1</sub> +3v <sub>2</sub> <sup>1</sup> - v <sub>2</sub> <sup>1</sup>	1381.2141	297.00(17)
d	R(6)	4983.19099	v <sub>2</sub> <sup>1</sup> +2v <sub>3</sub>	17.5982	296.01(15)
e	P(42)	4983.06430	3v <sub>1</sub> +2v <sub>2</sub>	756.1594	296.01(15)
f	P(43)	4981.82774	3v <sub>1</sub> +2v <sub>2</sub>	792.1383	296.36(7)
g	R(4)	4981.68812	v <sub>2</sub> <sup>1</sup> +2v <sub>3</sub>	8.3802	296.36(7)
h	P(44)	4980.58112	3v <sub>1</sub> +2v <sub>2</sub>	828.9513	296.32(5)

spectrum. The integrated absorbance and the central frequency of the probed lines, as well as the baseline parameters, are retained as free parameters in the individual spectra. Finally, the Doppler width is fixed at the value corresponding to the measured temperature,  $T$ , over the entire pressure range, according to the formula  $\Gamma_D = \frac{v_0}{c} \sqrt{2 \ln 2 \frac{k_B T}{M}}$ , being  $c$  the speed of light,  $k_B$  the Boltzmann constant, and  $M$  the molecular mass.

The measured spectra are compared to the selected line shape model with the aim to minimize residuals respect to the function of Eq. (7). This is done by using a nonlinear least square method with a Levenberg-Marquardt algorithm, implemented under the MATLAB environment. It is worth noting that no absolute stabilization of the laser frequency is performed. For this reason, spectral averaging is avoided since it could lead to a significant distortion of the experimental line shape.

#### 4. Path length determination

The measurement of the path length inside the MRC,  $L_{MRC}$ , is carried out following a procedure similar to that already described in detail elsewhere [41], except for few new experimental tricks that will be described hereafter. Briefly, the basic idea is to compare the integrated absorbance of a particular molecular transition recorded simultaneously at the outputs of the reference cell and the MRC, filled with a gaseous sample at the same thermodynamic conditions. At this purpose, we use the additional laser DFB-DL2 as described in Section 2. The optical path into the reference cell is determined to be  $L_{ref} = (1.012 \pm 0.001)$  m as explained in Ref. [41].

Since the N<sub>2</sub>O transitions are too weak for being observed in the reference cell, we use a CO<sub>2</sub> gas sample for the path length measurement. For carbon dioxide relatively strong absorption features can be found at the operation wavelengths. We record absorption spectra corresponding to the R(28) and R(29) transitions, at 4985.334523 and 4985.439252 cm<sup>-1</sup>, respectively. These transitions have comparable line strengths (of the order of  $3 \times 10^{-23}$  cm/molecule). The CO<sub>2</sub> doublet is carefully selected as the best compromise for the purposes of the path length determination. In fact, it guarantees enough signal-to-noise ratio for acquisitions performed in the reference cell, while avoiding a 100% fractional absorption in the MRC cell. The measurements are done for ten different carbon dioxide pressures, in the range 5–50 Torr. For each pressure, one hundred spectra are acquired. The spectral analysis is performed by means of the multispectrum approach previously described, using the qSDHC profile for both the lines. Moreover, taking advantage of the simultaneous presence of two lines in the entire laser scan, we could double the available integrated absorbance data. In summary, a total of 2000 integrated absorbance data are used for the path length determination. Examples of experimental absorbance data, for each of the two carbon dioxide lines, are plotted in the upper panel of Fig. 2, for all the spectral acquisitions. We perform a linear fit of the integrated absorbance

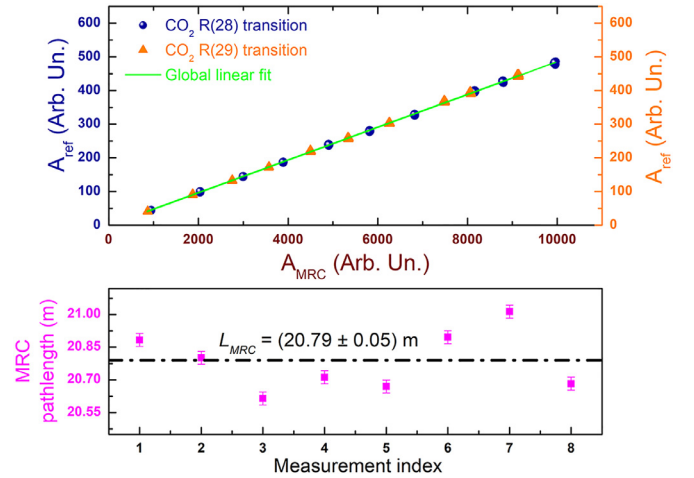


**Fig. 2.** Upper panel: plot of the integrated absorbance in the reference cell as a function of the same quantity in the multiple reflections cell, corresponding to the R(28) (blue circles) and R(29) (orange triangles) CO<sub>2</sub> transitions. The slope of the best-fit line is equal to the ratio between the reference and the MRC cell lengths. Lower panel: Repeated determinations of  $L_{MRC}$  performed in eight different days. Uncertainty bars are given by the propagation of the statistical uncertainty of  $\epsilon$  on  $L_{MRC}$  (see Section 6 for the contribution of  $L_{ref}$  to the uncertainty). (For interpretation of the references to colour in this figure legend, the reader is referred to the web version of this article.)

in the reference cell,  $A_{ref}$ , versus the corresponding quantity in the MRC,  $A_{MRC}$ . Particularly, two linear fits are performed, sharing, for both the transitions, the slope and the intercept. Finally, the MRC path length is retrieved according to the formula  $L_{MRC} = L_{ref}/\epsilon$ , being  $\epsilon$  the shared slope of the two straight lines. As shown in the lower panel of Fig. 2, we repeat this measurement procedure in eight different days, determining  $L_{MRC} = (20.79 \pm 0.05)$  m.

#### 5. Results and discussion

Fig. 3 provides information about the capability of the line shape models to reproduce the experimental spectra. The fit quality is expressed in terms of the mean reduced chi-square,  $\chi_r^2$ , and average root-mean-square value of the residuals, r.m.s. For each data set, the multispectrum fitting procedure involves 19 spectra across the entire pressure range, and it is repeated 100 times. The upper panel of Fig. 3 shows the average of 100 values of the global reduced chi-square for the qSDV, the qSDHC, and  $\beta$ HT profiles, along with their versions including line mixing. A weak dependence on the model can be noticed, with a minimum  $\chi_r^2$  of 1.06462 for the qSDV profile. Moreover, either the qSDHC or the  $\beta$ HT profile exhibit the same results. The inclusion of LM does not improve the quality of the fits, the  $\chi_r^2$  being about 0.2% higher than the case without LM. The lower panel of Fig. 3 shows that,

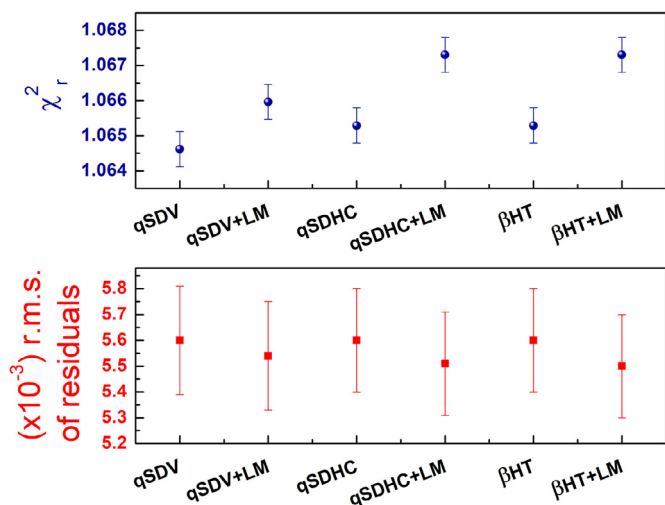


**Fig. 3.** Upper panel: Mean reduced chi-square values,  $\chi_r^2$ , as function of the adopted line shape models. Lower panel: Average root-mean-square values of the residuals (r.m.s.) in correspondence of the qSDV, qSDHC, and  $\beta$ HT profiles, along with their version including line mixing effects. For both the panels, data refer to the fits of the P(42) and R(6) lines pair.

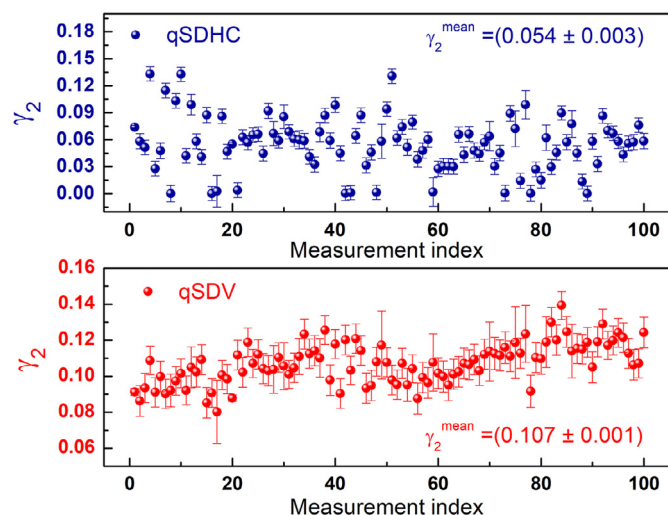


**Fig. 4.** Upper panel: Repeated determinations of the speed dependence of collisional broadening parameter for the P(42) transition as determined by the application of the qSDHC profile in Eq. (7). Uncertainty bars on data are the statistical errors as provided by the multispectrum analysis. Lower panel: Same quantities of the upper panel in the case of the qSDV model.

from the point of view of fits residuals, all the models are equivalent, the differences between r.m.s. of residuals being not statistically significant. We must note that, in the case of the qSDHC profile, the correlation index between the parameters  $\gamma_2$  and  $\nu_{VC}$ , as retrieved from the correlation matrix coming from the fitting procedure, is 0.57. The global approach effectively reduces correlation issues, making the retrieved parameters and their statistical uncertainties meaningful.

Regarding the spectroscopic parameters that could be retrieved from the fits, the discussion deserves a deeper understanding. In the well-known Berman-Pickett approach [42,43], the interaction potential between molecules is assumed of the form  $V(r) \sim 1/r^q$ , being  $r$  the intermolecular distance, and  $q$  a specific exponent describing the molecular interaction. When the speed dependence of the collisional broadening is modelled by means of a quadratic law, the  $\gamma_2$  parameter can be connected to the  $q$ -exponent by means of a confluent hypergeometric function [44]. The two panels of Fig. 4 reproduce the retrieved parameter of speed dependence of collisional broadening for the P(42) transition as obtained with the qSDHC (upper panel) and qSDV (lower panel) profiles. It is worth highlighting that due to the lower number of parameters, the statistical fluctuations from one set of spectra to the other are significantly reduced when the qSDV model is adopted. In the case of the qSDHC model,  $\gamma_2 = (0.054 \pm 0.003)$  corresponds to a  $q$ -exponent of about 3.91, whereas in the case of the qSDV profile  $\gamma_2$  increases up to  $(0.107 \pm 0.001)$ , leading to  $q = 8.80$ . Since  $\text{N}_2\text{O} - \text{N}_2\text{O}$  interaction potential is very similar to that of self-colliding  $\text{CO}_2$  [45], we could reasonably expect  $q$ -values that do not exceed 7 [34]. This means that the qSDV model leads to an overestimation of the narrowing due to speed dependence, with retrieved  $\gamma_2$ -values that are not physically meaningful. To further check the adequacy of the quadratic approximation, we repeated the spectral analysis for the P(42) transition by using a hypergeometric speed dependence for the collisional broadening. So doing, we obtained a  $q$ -exponent of  $(4.12 \pm 0.13)$  and a velocity-changing collision frequency per unit of pressure of  $(0.50 \pm 0.04)$  MHz/Torr. The two values are consistent, within the experimental uncertainties, with those provided by the qSDHC model. Similar results have been obtained for the other investigated transitions. The inclusion of LM does not change these outcomes.

If we compare the frequency of the velocity-changing collisions as retrieved by the  $\beta$ HT and the qSDHC models, we find that this latter returns values that are lower than those provided by the  $\beta$ -corrected profile. More precisely, for all the investigated transitions, the ratios of the two sets of  $\nu_{VC}$  values lie in the interval between 0.67 and 0.77, which is completely reasonable in the case of self-colliding  $\text{N}_2\text{O}$  spectra recorded in the 5–100 Torr pressure range at room temperature. This behavior agrees with the recent findings of Ref. [36].

We also investigate the influence of  $\eta$  in the spectral analysis. Whatever is the line shape adopted, when  $\eta$  is not fixed to zero and treated as a shared parameter among the spectra, the fitting procedure provides two opposite results. In particular, for some transitions  $\eta$  is negative, whereas for all the other the  $\eta$ -value makes the quantity  $(\nu_{VC} - \eta\Gamma_0) < 0$ . In both cases, this is a not physically meaningful [46], thus motivating our choice of using uncorrelated profiles.

All these outcomes allow us to claim that, in the entire investigated pressure range, the qSDHC model is the most appropriate choice in reproducing the experimental  $\text{N}_2\text{O}$  spectra. While preserving a good fit quality, it also assures a high fidelity in retrieving the  $\nu_{VC}$  and  $\gamma_2$  parameters. We must also note that, for all the models, the inclusion of line mixing effects does not translate into fits which show a better quality, being some of the retrieved molecular parameters not physically sounding.

Fig. 5 shows examples of line fitting by means of the qSDHC profile for a pair of spectral acquisitions at two different pressures, in coincidence with the P(42) and R(6) lines. The residuals result from the application of the multispectrum fitting procedure described in Section 3. We must note the excellent agreement between the experimental data and the theoretical model, the r.m.s. of the residuals being at the level of 0.005, mostly limited by the experimental noise. For all the other transitions, a similar level of agreement is found. No clear structures could be evidenced in the residuals, at any pressure. It is worth noting that no asymmetry in the recorded profiles could be noticed; this as a confirmation of the fact that the speed-dependence of pressure shifting could be neglected ( $\delta_2 = 0$ ).

To pass from integrated absorbance to line intensities, for each transition, we rescale the measured integrated absorbance  $A(T)$  to the reference temperature  $T_0 = 296$  K using the following

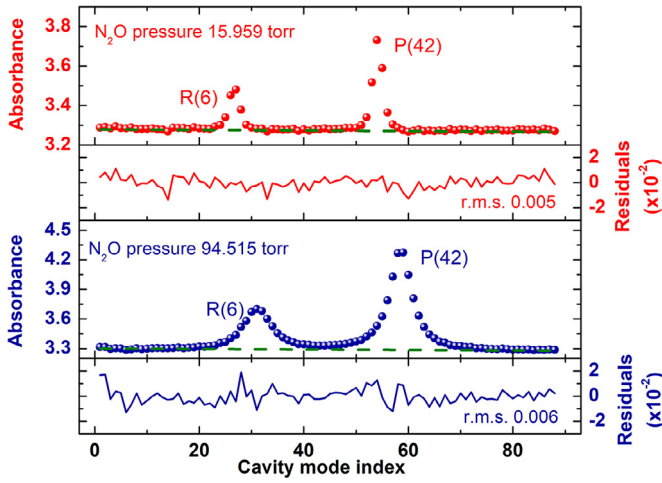


**Fig. 5.** Examples of an experimental spectra, corresponding to the P(42) and R(6) transitions, along with the residuals resulting from the application of the multispectrum fitting approach to a set of 19 spectra, across the pressure range between 5 and 100 Torr. The dashed lines represent the spectra baseline as retrieved from the multispectrum fitting.

equation:

$$A(T_0) = A(T) \frac{T}{T_0} \frac{Q(T)}{Q(T_0)} \exp \left[ - \frac{hcE''}{k_B} \left( \frac{1}{T_0} - \frac{1}{T} \right) \right], \quad (8)$$

where  $h$  is Planck constant,  $Q$  is the total internal partition function, and  $E''$  is the lower state energy level.  $Q$  is calculated according to the outcomes of Ref. [47], while  $E''$  (reported in the 4th column of Table 1) is taken from the HITRAN database. We then convert the pressure values to  $N_2O$  number densities according to the equation  $N = \kappa \left( \frac{p \times 10^{-6}}{k_B T} \right)$ , using the measured temperatures and pressures (in K and Pa, respectively), and the quoted purity of the  $N_2O$  gas bottle,  $\kappa$ . We assume an atmospheric isotopic abundance for the  $^{14}N_2^{16}O$  isotopologue (0.990333, as used in the HITRAN database). Next, we plot our  $A(T_0)$  values versus the number densities and fit the resulting points to a straight line by means of a weighted linear fit, as shown in Fig. 6 for the P(42) transition. The slope of the line is equal to  $1/(S_{LMRC})$ . Since  $L_{MRC}$  could be measured from the experimental procedure described in Section 4,  $S$  can be obtained. Concerning the contributions of  $A(T_0)$  and  $N$  to the uncertainty on  $S$ , we refer the readers to the discussion of Section 6. For the dataset of Fig. 6, we observe a good agreement between the linear behavior and the experimental points, being 0.9989 the linear correlation coefficient of the fit. Moreover, the application of an  $F$ -test returns a measured  $F$ -value,  $F_m$ , that is much greater than the critical  $F$ -value,  $F_c$ , calculated in correspondence to a confidence level of 99% and 1898 degrees of freedom. In particular, the probability that  $F_c \geq F_m$  is estimated to be only 0.002%. This circumstance allows us to affirm that the level of

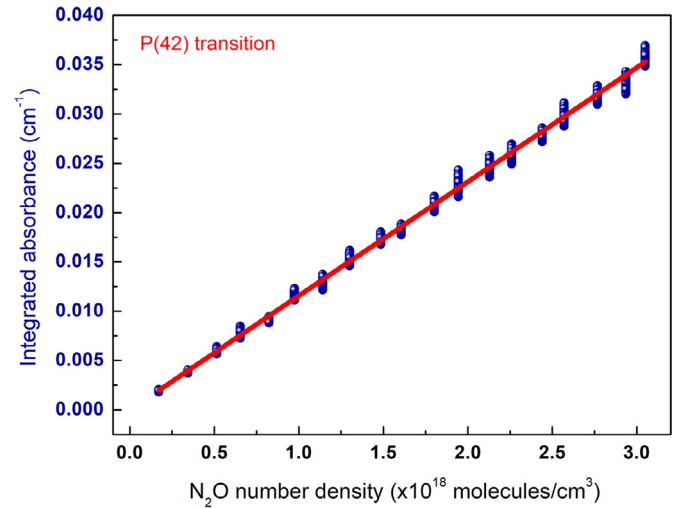


**Fig. 6.** Plot of the integrated absorbance as function of the molecular number density, along with the linear fit. For clarity, uncertainty bars on the absorbance data are not displayed. As expected, the intercept of the weighted best-fit line is well consistent with zero within the experimental uncertainty.

goodness for the weighted linear fit is more than satisfactory. We find similar agreements for all the investigated transitions.

The measured line intensities are given in the second and third columns of Table 2, for qSDHC and qSDV profiles, respectively. In these two columns, the number in parentheses represents the  $1-\sigma$  statistical uncertainty as retrieved by the weighted linear fit. The results provided by the two models agree within  $2-\sigma$  uncertainty, in most cases. The 4th and 5th columns report line strength values from the HITRAN [19] and NOSD-1000 [48] databases, respectively. We must note that, being the NOSD-1000 a database developed for high-temperature applications, line intensities have been calculated at a temperature of 1000 K. For the purposes of this study, we rescaled them to the temperature  $T_0$ . The sixth column lists the relative deviations between the experimental determinations obtained with the qSDHC and qSDV profiles, ranging between  $-0.23$  to  $0.29\%$ , while the last two columns report the same quantities calculated for the qSDHC model with respect to the values of the two databases. It turns out that the level of agreement is more satisfactory for the NOSD-1000 database, rather than HITRAN. In particular, in the case of NOSD-1000, the relative deviation spans from  $-2.76$  to  $2.57\%$ , while the r.m.s. of the deviations is  $1.84\%$ . As for the HITRAN database, we should note that most of our determinations are larger than those reported in HITRAN, the r.m.s. value of the relative differences amounting to  $2.10\%$ . It is worth pointing out that authors of Ref. [12] provided line intensities for some of the transitions investigated in the present work. In particular, for the “a”, “d”, “e”, “f” and “g” lines (see Table 1 for correspondence with the transitions and their vibrational assignment), we find a

**Table 2**  
Measured line intensities as obtained by means of the qSDHC and qSDV profiles in comparison with values from databases.

Line	$S \times 10^{-24}$ (cm/molecule)				Relative deviation (%)		
	qSDHC	qSDV	HITRAN [19]	NOSD1000 [48]	qSDHC-qSDV	qSDHC-HITRAN	qSDHC-NOSD1000
a	6.227(7)	6.209(7)	6.371	6.399	0.29	-2.31	-2.76
b	3.192(4)	3.186(4)	3.072	3.183	0.19	3.76	0.28
c	0.267(1)	0.265(1)	0.269	0.265	0.75	-0.56	0.67
d	2.834(2)	2.833(2)	2.814	2.912	0.04	0.71	-2.75
e	5.546(3)	5.559(3)	5.524	5.540	-0.23	0.40	0.11
f	4.835(4)	4.839(4)	4.758	4.776	-0.08	1.59	1.22
g	2.280(2)	2.281(2)	2.210	2.285	-0.04	3.07	-0.22
h	4.206(2)	4.213(2)	4.072	4.098	-0.17	3.19	2.57

**Table 3**

Measured self-broadening coefficients along with values from HITRAN database. The last two columns list the quadratic speed-dependence parameters and the frequencies of the velocity-changing collisions per unit of pressure as retrieved using the qSDHC profile.

Line	$\gamma_{self}$ (MHz/Torr)			Relative deviation (%)		$\gamma_2$	$\bar{\nu}_{VC}$ (MHz/Torr)
	qSDHC	qSDV	HITRAN	qSDHC-qSDV	qSDHC-HITRAN		qSDHC
a	3.249(4)	3.214(4)	3.274	1.08	−0.77	0.058(7)	0.45(6)
b	4.239(7)	4.248(7)	4.379	−0.21	−3.31	0.087(7)	0.35(12)
c	2.734(7)	2.735(7)	3.253	−0.04	−18.9	0.009(7)	0.52(9)
d	4.131(3)	4.132(3)	4.418	−0.02	−6.92	0.089(2)	0.32(11)
e	3.240(3)	3.265(3)	3.274	−0.77	−1.05	0.054(3)	0.49(3)
f	3.265(3)	3.278(3)	3.235	−0.40	0.92	0.081(5)	0.27(5)
g	4.548(6)	4.552(6)	4.536	−0.09	0.27	0.061(3)	0.30(10)
h	3.269(2)	3.307(2)	3.235	−1.16	1.03	0.023(4)	0.56(4)

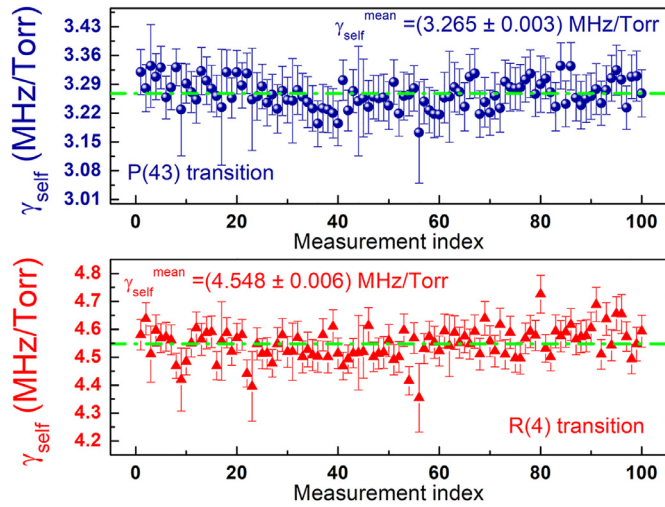


**Fig. 7.** Upper panel: Self-broadening coefficient determinations for the P(43) transition using the qSDHC profile. The green dashed-dotted line represents the  $\gamma_{self}$  mean value. Uncertainty bars on data are the statistical errors as provided by the multispectrum analysis. Lower panel: Same quantities of the upper panel for the R(4) line. (For interpretation of the references to colour in this figure legend, the reader is referred to the web version of this article.)

deviation respect to their determinations at the level of 2.89% (calculated as r.m.s. of the relative differences), which is comparable with the uncertainty of 2.5% reported in [12].

The application of the global analysis allows us to determine the self-broadening coefficient,  $\gamma_{self} = \Gamma_0/p$ , the quadratic speed-dependence parameter, and the frequencies of the velocity-changing collisions per unit of pressure, for all the investigated transitions. Table 3 summarizes the results we obtained, while Fig. 7 shows, in the upper and lower panels, examples of  $\gamma_{self}$  determinations for the “f” and “g” transitions, respectively. In Table 3, the second and the third columns refer to the  $\gamma_{self}$  measured values as obtained by means of the qSDHC and qSDV profiles, while the 4th column reports the data of the HITRAN database. As a matter of fact,  $\gamma_{self}$ -values have been rescaled to the reference temperature according to the equation  $\gamma_{self}(T_0) = \gamma_{self}(T)(T/T_0)^{0.75}$ . The 5th and 6th columns, instead, report the relative difference between determinations obtained with the two line shape models and those resulting from a comparison of the qSDHC profile with HITRAN values, respectively. As it could be expected, in most cases the qSDV model overestimates the pressure broadening contribution as compared to the qSDHC model, thus confirming the outcomes previously discussed. As for the comparison with the HITRAN database, relatively large deviations are observed for the “b”,

**Table 4**

Uncertainty budget (in terms of relative contributions, corresponding to one standard deviation) related to the spectroscopic determination of line intensities.

Relative contribution	Type A (%)	Type B (%)
Weighted linear fit	0.13	
Path length	0.24	0.10
Pressure		0.12
Temperature		0.06
Line shape model		0.19
Partition function		0.04
Detectors' non-linearity		0.04
Frequency scale		0.03
Laser-emission width		Negligible
Overall uncertainty		0.38%

“c” and “d” lines. For the other lines, the agreement is quite satisfactory.

Finally, in the last two columns, we list the  $\gamma_2$  and the velocity-changing collisions per unit of pressure,  $\bar{\nu}_{VC} = \nu_{VC}/p$ , parameters. The quadratic speed-dependence parameters sound reasonable for all the transitions, being consistent with a  $q$ -exponent roughly varying between 3 and 6, the former typical of a dipole-dipole interaction, the latter occurring for a dipole-induced dipole force. The  $\bar{\nu}_{VC}$ -values are in all the cases lower than the  $N_2O$  self-diffusion coefficient at the working temperature [49].

## 6. Uncertainty budget

In this Section, we report on the complete uncertainty budget in line strength determinations. We will make use of the well-recognized distinction between type A and type B uncertainties. The former are evaluated based on statistical method for treating data, while the latter are inferred from scientific judgment or other information concerning the possible values of the quantity. Usually, type B includes also systematic deviations. Table 4 summarizes the complete uncertainty budget.

A first source of type A uncertainty corresponds to the statistical uncertainty of the weighted linear fits (similar to that of Fig. 6). As reported in Table 2, this contribution ranges between 0.05 to 0.37%, depending on the selected  $N_2O$  line. In particular, excluding the weakest transition, we take as type A uncertainty the largest value that was observed, namely, 0.13%, corresponding to the case of the R(7) transition. A second contribution of the type A is related to the optical path length. In particular, the reproducibility of its determination (see lower panel of Fig. 2) can be estimated to be 0.24%, making this contribution the most important in the whole budget.



Type B contributions can be ascribed to seven different sources, namely (i) the pressure, (ii) the temperature, (iii) the influence of the line shape model, (iv) the optical path length, (v) the partition function, (vi) the detector non-linearity, and (vii) the frequency scale. More specifically, the pressure uncertainty is 0.12%, a combination of the predominant uncertainty on the purity of the gas sample, accuracy of our pressure gauge, and deviation from the natural abundance. The uncertainty on the purity of the gas sample was 0.1%, as certified by the company manufacturing the cylinder. The accuracy of the pressure gauge was 0.05%. As for the uncertainty related to the abundances of the different isotopologues, it is estimated under the hypothesis that the  $\text{N}_2\text{O}$  gas sample stems from normal terrestrial material, without modifications of its isotopic makeup. We assumed that the uncertainties in the isotopic composition of the elements are those published by the International Union of Pure and Applied Chemistry (IUPAC) and given in Ref. [50]. In particular, for  $^{14}\text{N}$  and  $^{16}\text{O}$  they are 0.02 and 0.016%, respectively. These values lead to a relative uncertainty associated to deviations from the natural abundance of 0.03%. As for the cell's temperature, we remind that no active stabilization is implemented in our experimental setup. For this reason, the temperature is continuously recorded by means of a calibrated thermometer, in each measurements' run. Thus, the temperature uncertainty is calculated as the relative variation during a complete set of measurements, amounting to 0.06%. Regarding the influence of the adopted line shape model to the uncertainty, we can benefit of the arguments done in Section 5. In that occasion, we found that the r.m.s. value of the relative differences in the retrieved line intensities due to the use of two different profiles, namely the qSDHC and qSDV, amounts to 0.19%. Adopting a very cautious approach, this quantity can be considered as the line shape contribution to the budget of uncertainties. It is worth noting that the results provided by the  $\beta\text{HT}$  profile well agree with those obtained by means of the qSDHC model. The type B component associated to the optical path length amounts to 0.10%, due to the uncertainty of  $L_{\text{ref}}$ . Since the partition function comes into play during the rescaling of the integrated absorbance to the reference temperature (see Eq. (8)), its uncertainty must be properly taken into account. Following the outcomes of Ref. [47], we determine that this additional uncertainty is 0.04%. As for the last two contributions, following the same procedure described in Ref. [25], we quantify the uncertainties due to the detector non-linearity and frequency scale calibration to be 0.04% and 0.03%, respectively.

It is worth noting that the OF-LAS technique assures that any systematic influence in the line strength determinations ascribable to the spectral purity of the probe laser can be completely neglected, being the laser-emission width below the 10-kHz level, namely, at least a factor  $5 \times 10^{-5}$  smaller than the width of the absorption line in the worst case.

Finally, adding in quadrature all the contributions, the upper limit to the  $1-\sigma$  relative uncertainty of the measured line intensities of 0.38% is obtained.

## 7. Conclusions

In conclusion, we performed measurements of eight self-broadened  $\text{N}_2\text{O}$  transitions in the  $2\mu\text{m}$  spectral region by means of the OF-LAS technique in conjunction with the use of a multiple reflections cell. Incorporating into the experimental setup a self-referenced optical frequency comb for highly accurate frequency scale calibration and adopting a global analysis approach in the fitting of the experimental spectra, we are able to determine line intensities with an overall uncertainty within 0.38%. We compared our line strength determinations with data provided by the NOSD-1000 and HITRAN databases the agreement being slightly better with the former rather than the latter.

High spectral fidelity allows us to test the most advanced line shape models, also those including line mixing effects, recognizing the quadratic speed dependent hard collision model (a symmetric and uncorrelated version of the Hartmann-Tran profile) as the best choice in capturing collisional effects. It allows to successfully model the measured spectra at almost the level of the experimental noise, over the whole investigated pressure range, preserving the accuracy of the retrieved line shape parameters. To the best of our knowledge, this is the first demonstration that the mechanisms of collisional narrowing and speed-dependent effects simultaneously contribute to  $\text{N}_2\text{O}$  line shapes at  $2\mu\text{m}$  wavelength. This strongly supports the recent choice of implementing the Hartmann-Tran as the standardized profile in the HITRAN database for atmospheric relevant molecules.

## Declaration of Competing Interest

The authors declare that they have no known competing financial interests or personal relationships that could have appeared to influence the work reported in this paper.

## CRediT authorship contribution statement

**T.A. Odintsova:** Investigation, Data curation. **E. Fasci:** Investigation, Validation. **S. Gravina:** Investigation. **L. Gianfrani:** Conceptualization, Writing - review & editing, Supervision, Funding acquisition. **A. Castrillo:** Conceptualization, Formal analysis, Writing - original draft, Writing - review & editing.

## Acknowledgments

T.A.O. thanks Università degli Studi della Campania "Luigi Vanvitelli" for the kind hospitality and support in the framework of the 2019 Visiting Professors call. This research was performed under the program V:ALERE plus, VANviteLLi pEr la RicErca, call 2018, funded by Università degli Studi della Campania "Luigi Vanvitelli".

## Supplementary material

Supplementary material associated with this article can be found, in the online version, at doi:[10.1016/j.jqsrt.2020.107190](https://doi.org/10.1016/j.jqsrt.2020.107190).

## References

- [1] Meure CM, Etheridge D, Trudinger C, Steele P, Langenfelds R, van Ommen T, Smith A, Elkins J. Law dome  $\text{CO}_2$ ,  $\text{CH}_4$  and  $\text{N}_2\text{O}$  ice core records extended to 2000 years BP. *Geophys Res Lett* 2006;33(14):L14810. doi:[10.1029/2006GL026152](https://doi.org/10.1029/2006GL026152).
- [2] Yung YL, Wang WC, Lacis AA. Greenhouse effect due to atmospheric nitrous oxide. *Geophys Res Lett* 1976;3(10):619–21. doi:[10.1029/GL003i010p00619](https://doi.org/10.1029/GL003i010p00619).
- [3] Griffis TJ, Chen Z, Baker JM, Wood JD, Millet DB, Lee X, Venterea RT, Turner PA. Nitrous oxide emissions are enhanced in a warmer and wetter world. *Proc Natl Acad Sci* 2017;114(45):12081–5. doi:[10.1073/pnas.1704552114](https://doi.org/10.1073/pnas.1704552114).
- [4] Prather MJ, Hsu J, DeLuca NM, Jackman CH, Oman LD, Douglass AR, Fleming EL, Strahan SE, Steenrod SD, Svde OA, Isaksen ISA, Froidevaux L, Funke B. Measuring and modeling the lifetime of nitrous oxide including its variability. *J Geophys Res* 2015;120(11):5693–705. doi:[10.1002/2015JD023267](https://doi.org/10.1002/2015JD023267).
- [5] Bouwman AF, Hoek KWVd, Olivier JGJ. Uncertainties in the global source distribution of nitrous oxide. *J Geophys Res* 1995;100(D2):2785–800. doi:[10.1029/94JD02946](https://doi.org/10.1029/94JD02946).
- [6] Ravishankara AR, Daniel JS, Portmann RW. Nitrous oxide ( $\text{N}_2\text{O}$ ): the dominant ozone-depleting substance emitted in the 21st century. *Science* 2009;326(5949):123–5. doi:[10.1126/science.1176985](https://doi.org/10.1126/science.1176985).
- [7] Wunch D, Toon GC, Blavier J-FL, Washenfelder RA, Notholt J, Connor BJ, Griffith DWT, Sherlock V, Wennberg PO. The total carbon column observing network. *Philos Trans R Soc A* 2011;369(1943):2087–112. doi:[10.1098/rsta.2010.0240](https://doi.org/10.1098/rsta.2010.0240).
- [8] De Mazière M, Thompson AM, Kurylo MJ, Wild JD, Bernhard G, Blumenstock T, Braathen GO, Hannigan JW, Lambert J-C, Leblanc T, McGee TJ, Nedoluha G, Petropavlovskikh I, Seckmeyer G, Simon PC, Steinbrecht W, Strahan SE. The network for the detection of atmospheric composition change (NDACC): history, status and perspectives. *Atmos Chem Phys* 2018;18(7):4935–64. doi:[10.5194/acp-18-4935-2018](https://doi.org/10.5194/acp-18-4935-2018).

- [9] Waters JW, Froidevaux L, Harwood RS, Jarnot RF, Pickett HM, Read WG, Siegel PH, Cofield RE, Filipiak MJ, Flower DA, Holden JR, Lau GK, Livesey NJ, Manney GL, Pumphrey HC, Santee ML, Wu DL, Cuddy DT, Lay RR, Loo MS, Perun VS, Schwartz MJ, Stek PC, Thurstans RP, Boyles MA, Chandra KM, Chavez MC, Chen G-S, Chudasama BV, Dodge R, Fuller RA, Girard MA, Jiang JH, Jiang Y, Knosp BW, LaBelle RC, Lam JC, Lee KA, Miller D, Oswald JE, Patel NC, Pukala DM, Quintero O, Scaff DM, Snyder WV, Tope MC, Wagner PA, Walch MJ. The earth observing system microwave limb sounder (EOS MLS) on the aura satellite. *IEEE Trans Geosci Remote Sens* 2006;44(5):1075–92. doi:[10.1109/TGRS.2006.873771](https://doi.org/10.1109/TGRS.2006.873771).
- [10] Toth RA. Line positions and strengths of N<sub>2</sub>O between 3515 and 7800 cm<sup>-1</sup>. *J Mol Spectrosc* 1999;197(2):158–87. doi:[10.1006/jmsp.1999.7907](https://doi.org/10.1006/jmsp.1999.7907).
- [11] Toth RA. N<sub>2</sub>- and air-broadened linewidths and frequency-shifts of N<sub>2</sub>O. *J Quant Spectrosc Radiat Transf* 2000;66(3):285–304. doi:[10.1016/S0022-4073\(99\)00167-3](https://doi.org/10.1016/S0022-4073(99)00167-3).
- [12] Daumont L, Auwera J, Teffo J-L, Perevalov V, Tashkun S. Line intensity measurements in <sup>14</sup>N<sub>2</sub><sup>16</sup>O and their treatment using the effective dipole moment approach: i. the 4300- to 5200- cm<sup>-1</sup> region. *J Mol Spectrosc* 2001;208(2):281–91. doi:[10.1006/jmsp.2001.8400](https://doi.org/10.1006/jmsp.2001.8400).
- [13] Loos J, Birk M, Wagner G. Pressure broadening, -shift, speed dependence and line mixing in the ν<sub>3</sub> rovibrational band of N<sub>2</sub>O. *J Quant Spectrosc Radiat Transf* 2015;151:300–9. doi:[10.1016/j.jqsrt.2014.10.008](https://doi.org/10.1016/j.jqsrt.2014.10.008).
- [14] Predoi-Cross A, Hashemi R, Devi VM, Naseri H, Smith MAH. Analysis of Fourier transform spectra of N<sub>2</sub>O in the ν<sub>3</sub> band for atmospheric composition retrievals. *Can J Phys* 2018;96(4):454–64. doi:[10.1139/cjp-2017-0303](https://doi.org/10.1139/cjp-2017-0303).
- [15] Wang L, Perevalov V, Tashkun S, Gao B, Hao L-Y, Hu SM. Fourier transform spectroscopy of N<sub>2</sub>O weak overtone transitions in the 1–2 μm region. *J Mol Spectrosc* 2006;237(2):129–36. doi:[10.1016/j.jms.2006.03.007](https://doi.org/10.1016/j.jms.2006.03.007).
- [16] Werwein V, Brunzendorf J, Serdyukov A, Werhahn O, Ebert V. First measurements of nitrous oxide self-broadening and self-shift coefficients in the 0002-0000 band at 2.26 μm using high resolution fourier transform spectroscopy. *J Mol Spectrosc* 2016;323:28–42. doi:[10.1016/j.jms.2016.01.010](https://doi.org/10.1016/j.jms.2016.01.010). Atmospheric Spectroscopy
- [17] Werwein V, Brunzendorf J, Li G, Serdyukov A, Werhahn O, Ebert V. High-resolution Fourier transform measurements of line strengths in the 0002-0000 main isotopologue band of nitrous oxide. *Appl Opt* 2017;56(11):E99–E105. doi:[10.1364/AO.56.000E99](https://doi.org/10.1364/AO.56.000E99).
- [18] Margottin-Maclou M, Henry A, Valentin A. Line mixing in the Q branches of the ν<sub>1</sub> + ν<sub>2</sub> band of nitrous oxide and of the (1110) ← (0220) band of carbon dioxide. *J Chem Phys* 1992;96(3):1715–23. doi:[10.1063/1.462126](https://doi.org/10.1063/1.462126).
- [19] Gordon I, Rothman L, Hill C, Kochanov R, Tan Y, Bernath P, Birk M, Boudon V, Campargue A, Chance K, Drouin B, Flaud J-M, Gamache R, Hodges J, Jacquemart D, Perevalov V, Perrin A, Shine K, Smith M-A, Tennyson J, Toon G, Tran H, Tyuterev V, Barbe A, Cossart A, Devi V, Furtenbacher T, Harrison J, Hartmann J-M, Jolly A, Johnson T, Karman T, Kleiner I, Kyuberis A, Loos J, Lyulin O, Massie S, Mikhailenko S, Moazzen-Ahmadi N, Miller H, Naumenko O, Nikitin A, Polyansky O, Rey M, Rotger M, Sharpe S, Sung K, Starikova E, Tashkun S, Auwera JV, Wagner G, Wilzewski J, Wcislo P, Yu S, Zak E. The HITRAN2016 molecular spectroscopic database. *J Quant Spectrosc Radiat Transf* 2017;203:3–69. doi:[10.1016/j.jqsrt.2017.06.038](https://doi.org/10.1016/j.jqsrt.2017.06.038).
- [20] Tashkun S, Perevalov V, Karlovets E, Kassi S, Campargue A. High sensitivity cavity ring down spectroscopy of N<sub>2</sub>O near 1.22 μm: (II) <sup>14</sup>N<sub>2</sub><sup>16</sup>O line intensity modeling and global fit of <sup>14</sup>N<sub>2</sub><sup>18</sup>O line positions. *J Quant Spectrosc Radiat Transf* 2016;176:62–9. doi:[10.1016/j.jqsrt.2016.02.020](https://doi.org/10.1016/j.jqsrt.2016.02.020).
- [21] Karlovets E, Lu Y, Mondelain D, Kassi S, Campargue A, Tashkun S, Perevalov V. High sensitivity CW-cavity ring down spectroscopy of N<sub>2</sub>O between 6950 and 7653 cm<sup>-1</sup> (1.44–1.31 μm): II. line intensities. *J Quant Spectrosc Radiat Transf* 2013;117:81–7. doi:[10.1016/j.jqsrt.2012.11.003](https://doi.org/10.1016/j.jqsrt.2012.11.003).
- [22] Karlovets E, Campargue A, Kassi S, Perevalov V, Tashkun S. High sensitivity cavity ring down spectroscopy of N<sub>2</sub>O near 1.22 μm: (i) rovibrational assignments and band-by-band analysis. *J Quant Spectrosc Radiat Transf* 2016;169:36–48. doi:[10.1016/j.jqsrt.2015.09.012](https://doi.org/10.1016/j.jqsrt.2015.09.012).
- [23] Wcislo P, Gordon I, Tran H, Tan Y, Hu S-M, Campargue A, Kassi S, Romanini D, Hill C, Kochanov R, Rothman L. The implementation of non-Voigt line profiles in the HITRAN database: H<sub>2</sub> case study. *J Quant Spectrosc Radiat Transf* 2016;177:75–91. doi:[10.1016/j.jqsrt.2016.01.024](https://doi.org/10.1016/j.jqsrt.2016.01.024).
- [24] Domyslawska J, Wjtewicz S, Maslowski P, Bielska K, Cygan A, Slowinski M, Trawinski RS, Ciurylo R, Lisak D. Line-shape analysis for high J R-branch transitions of the oxygen b band. *J Quant Spectrosc Radiat Transf* 2020;242:106789. doi:[10.1016/j.jqsrt.2019.106789](https://doi.org/10.1016/j.jqsrt.2019.106789).
- [25] Odintsova TA, Fasci E, Moretti L, Zak EJ, Polyansky OL, Tennyson J, Gianfrani L, Castrillo A. Highly accurate intensity factors of pure CO<sub>2</sub> lines near 2 μm. *J Chem Phys* 2017;146(24):244309. doi:[10.1063/1.4989925](https://doi.org/10.1063/1.4989925).
- [26] Morville J, Kassi S, Chenevier M, Romanini D. Fast, low-noise, mode-by-mode, cavity-enhanced absorption spectroscopy by diode-laser self-locking. *Appl Phys B* 2005;80:1027–38. doi:[10.1007/s00340-005-1828-z](https://doi.org/10.1007/s00340-005-1828-z).
- [27] Wehr R, Kassi S, Romanini D, Gianfrani L. Optical feedback cavity-enhanced absorption spectroscopy for in situ measurements of the ratio <sup>13</sup>C:<sup>12</sup>C in CO<sub>2</sub>. *Appl Phys B* 2008;92:459–65. doi:[10.1007/s00340-008-3086-3](https://doi.org/10.1007/s00340-008-3086-3).
- [28] Ngo N, Lisak D, Tran H, Hartmann JM. An isolated line-shape model to go beyond the Voigt profile in spectroscopic databases and radiative transfer codes. *J Quant Spectrosc Radiat Transf* 2013;129:89–100. doi:[10.1016/j.jqsrt.2013.05.034](https://doi.org/10.1016/j.jqsrt.2013.05.034).
- [29] Lisak D, Havey DK, Hodges JT. Spectroscopic line parameters of water vapor for rotation-vibration transitions near 7180 cm<sup>-1</sup>. *Phys Rev A* 2009;79:052507. doi:[10.1103/PhysRevA.79.052507](https://doi.org/10.1103/PhysRevA.79.052507).
- [30] De Vizia MD, Rohart F, Castrillo A, Fasci E, Moretti L, Gianfrani L. Speed-dependent effects in the near-infrared spectrum of self-colliding H<sub>2</sub><sup>18</sup>O molecules. *Phys Rev A* 2011;83:052506. doi:[10.1103/PhysRevA.83.052506](https://doi.org/10.1103/PhysRevA.83.052506).
- [31] Forthomme D, Cich M, Twagirayezu S, Hall G, Sears T. Application of the Hartmann-Ran profile to precise experimental data sets of <sup>12</sup>C<sub>2</sub>H<sub>2</sub>. *J Quant Spectrosc Radiat Transf* 2015;165:28–37. doi:[10.1016/j.jqsrt.2015.06.013](https://doi.org/10.1016/j.jqsrt.2015.06.013).
- [32] Fasci E, Odintsova TA, Castrillo A, De Vizia MD, Merlone A, Bertiglia F, Moretti L, Gianfrani L. Dual-laser absorption spectroscopy of C<sub>2</sub>H<sub>2</sub> at 1.4 μm. *Phys Rev A* 2016;93:042513. doi:[10.1103/PhysRevA.93.042513](https://doi.org/10.1103/PhysRevA.93.042513).
- [33] Polyansky OL, Bielska K, Ghysels M, Lodi L, Zobov NF, Hodges JT, Tennyson J. High-accuracy CO<sub>2</sub> line intensities determined from theory and experiment. *Phys Rev Lett* 2015;114:243001. doi:[10.1103/PhysRevLett.114.243001](https://doi.org/10.1103/PhysRevLett.114.243001).
- [34] Casa G, Wehr R, Castrillo A, Fasci E, Gianfrani L. The line shape problem in the near-infrared spectrum of self-colliding CO<sub>2</sub> molecules: experimental investigation and test of semiclassical models. *J Chem Phys* 2009;130(18):184306. doi:[10.1063/1.3125965](https://doi.org/10.1063/1.3125965).
- [35] Tennyson J, Bernath PF, Campargue A, Császár AG, Daumont L, Gamache RR, Hodges JT, Lisak D, Naumenko OV, Rothman LS, Tran H, Zobov NF, Buldyreva J, Boone CD, Vizia MDD, Gianfrani L, Hartmann J-M, McPheat R, Weidmann D, Murray J, Ngo NH, Polyansky OL. Recommended isolated-line profile for representing high-resolution spectroscopic transitions (IUPAC Technical Report). *Pure Appl Chem* 2014;86:1931–43. doi:[10.1515/pac-2014-0208](https://doi.org/10.1515/pac-2014-0208).
- [36] Konefal M, Slowinski M, Zaborowski M, Ciurylo R, Lisak D, Wcislo P. Analytical-function correction to the Hartmann-Tran profile for more reliable representation of the dicke-narrowed molecular spectra. *J Quant Spectrosc Radiat Transf* 2020;242:106784. doi:[10.1016/j.jqsrt.2019.106784](https://doi.org/10.1016/j.jqsrt.2019.106784).
- [37] Ciurylo R, Lisak D, Szudy J. Role of velocity- and speed-changing collisions on speed-dependent line shapes of H<sub>2</sub>. *Phys Rev A* 2002;66:032701. doi:[10.1103/PhysRevA.66.032701](https://doi.org/10.1103/PhysRevA.66.032701).
- [38] Rosenkranz P. Shape of the 5 mm oxygen band in the atmosphere. *IEEE Trans Antennas Propag* 1975;23(4):498–506. doi:[10.1109/TAP.1975.1141119](https://doi.org/10.1109/TAP.1975.1141119).
- [39] Rohart F, Mäder H, Nicolaisen HW. Speed dependence of rotational relaxation induced by foreign gas collisions: studies on CH<sub>3</sub>F by millimeter wave coherent transients. *J Chem Phys* 1994;101(8):6475–86. doi:[10.1063/1.468342](https://doi.org/10.1063/1.468342).
- [40] Amodio P, Moretti L, Castrillo A, Gianfrani L. Line-narrowing effects in the near-infrared spectrum of water and precision determination of spectroscopic parameters. *J Chem Phys* 2014;140(4):044310. doi:[10.1063/1.4862482](https://doi.org/10.1063/1.4862482).
- [41] Castrillo A, Gagliardi G, Casa G, Gianfrani L. Combined interferometric and absorption-spectroscopic technique for determining molecular line strengths: applications to CO<sub>2</sub>. *Phys Rev A* 2003;67:062503. doi:[10.1103/PhysRevA.67.062503](https://doi.org/10.1103/PhysRevA.67.062503).
- [42] Berman PR. Speed-dependent collisional width and shift parameters in spectral profiles. *J Quant Spectrosc Radiat Transf* 1972;12(9):1331–42. doi:[10.1016/0022-4073\(72\)90189-6](https://doi.org/10.1016/0022-4073(72)90189-6).
- [43] Pickett HM. Effects of velocity averaging on the shapes of absorption lines. *J Chem Phys* 1980;73(12):6090–4. doi:[10.1063/1.440145](https://doi.org/10.1063/1.440145).
- [44] De Vizia MD, Castrillo A, Fasci E, Moretti L, Rohart F, Gianfrani L. Speed dependence of collision parameters in the H<sub>2</sub><sup>18</sup>O near-IR spectrum: experimental test of the quadratic approximation. *Phys Rev A* 2012;85:062512. doi:[10.1103/PhysRevA.85.062512](https://doi.org/10.1103/PhysRevA.85.062512).
- [45] Crusius J-P, Hellmann R, Hassel E, Bich E. *Ab initio* intermolecular potential energy surface and thermophysical properties of nitrous oxide. *J Chem Phys* 2015;142(24):244307. doi:[10.1063/1.4922830](https://doi.org/10.1063/1.4922830).
- [46] Domyslawska J, Wójtecz S, Cygan A, Bielska K, Lisak D, Maslowski P, Trawinski RS, Ciurylo R. Low-pressure line-shape study in molecular oxygen with absolute frequency reference. *J Chem Phys* 2013;139(19):194312. doi:[10.1063/1.4830219](https://doi.org/10.1063/1.4830219).
- [47] Gamache RR, Roller C, Lopes E, Gordon IE, Rothman LS, Polyansky OL, Zobov NF, Kyuberis AA, Tennyson J, Yurchenko SN, Cossart AG, Furtenbacher T, Huang X, Schwenke DW, Lee TJ, Drouin BJ, Tashkun SA, Perevalov VI, Kochanov RV. Total internal partition sums for 166 isotopologues of 51 molecules important in planetary atmospheres: application to HITRAN2016 and beyond. *J Quant Spectrosc Radiat Transf* 2017;203:70–87. doi:[10.1016/j.jqsrt.2017.03.045](https://doi.org/10.1016/j.jqsrt.2017.03.045).
- [48] Tashkun S, Perevalov V, Lavrentieva N. NOSD-1000, The high-temperature nitrous oxide spectroscopic databank. *J Quant Spectrosc Radiat Transf* 2016;177:43–8. doi:[10.1016/j.jqsrt.2015.11.014](https://doi.org/10.1016/j.jqsrt.2015.11.014).
- [49] Bird R, Stewart W, Lightfoot E. *Transport phenomena*. New York: Wiley; 2007.
- [50] Berglund M, Wieser ME. Isotopic compositions of the elements 2009 (IUPAC Technical Report). *Pure Appl Chem* 2011;83:347–410. doi:[10.1351/PAC-REP-10-06-02](https://doi.org/10.1351/PAC-REP-10-06-02).